AIAA 03–3464

Preliminary Work on DNS and LES of STBLI

M. Pino Martin, Sheng Xu and Minwei Wu
Department of Mechanical and Aerospace Engineering
Princeton University, Princeton, NJ

33rd AIAA Fluid Dynamics Conference and Exhibit
June 22–26, 2003/Orlando, FL

Preliminary Work on DNS and LES of STBLI

M. Pino Martin, Sheng Xu and Minwei Wu
Department of Mechanical and Aerospace Engineering
Princeton University, Princeton, NJ

Preliminary work on the development of a direct numerical and large-eddy simulation database of shockwave/turbulent boundary layer interaction is presented. These data will match the conditions of experiments being performed at the Gas Dynamics Laboratory at Princeton University. The canonical configurations chosen for the database and the simulation procedures to match the experimental conditions are described in this paper.

Introduction

Many aspects of shock/turbulent boundary layer interaction (STBLI) are not fully understood, including the dynamics of shock unsteadiness; turbulence amplification and mean flow modification induced by shock distortion; separation and reattachment criteria as well as the unsteady heat transfer near the separation and reattachment points; generation of turbulent mixing layers and underexpanded jets in the interaction region, especially when they impinge on a surface. Most importantly, we need to accurately predict the skin friction and heat transfer, given that the usual Reynolds analogies can lead to highly inaccurate results.[1] If we cannot predict the flow conditions we cannot expect to control them. Accurate predictions and scaling laws, and effective means to control the interaction regions can only be achieved by understanding the fundamental physics governing the dynamics of shockwave/turbulent boundary layer interactions.

We are working closely with experimentalists at the Gas Dynamics Laboratory at Princeton University to develop a detailed database of shockwave/turbulent boundary layer interaction. The experimental data will be used to validate the simulation data. In turn the numerical database will be used to complement the experiments in understanding the shockwave/turbulent boundary layer interaction phenomena.

Matching the experimental and computational Reynolds number, Re_θ, and skin friction, C_f, is challenging. The experiments must be performed at low Reynolds numbers so that the conditions can be accurately simulated via direct numerical simulation (DNS) and large-eddy simulation (LES). In addition, the initialization procedure and boundary conditions for the simulated incoming turbulent boundary layers must be accurate and efficient so that the values of Re_θ and C_f after the simulation transients can be controlled to match those of the experiment.

In this paper, we describe the three canonical configurations that we have chosen to study the interaction. The numerical method, computational grids and the initialization and inflow generation procedures are described.

Flow Configurations

Case I: Compression corner with separation

Although a large number of experiments already exist, none is suitable for comparison with DNS data, primarily because of large discrepancies in Reynolds number. We will use a 20° wedge to generate a two-dimensional, separated, compression corner interaction at Mach 3 and $Re_\theta = 3000$. Adams[2] performs a direct numerical simulation of this configuration at Mach 4 and $Re_\theta = 1685$.

Case II: Reflected shock case with separation and turbulent slip layer

This flow configuration is representative of a shock/turbulent boundary layer interaction occurring on the internal surface of a supersonic engine inlet or on the wall inside a scramjet engine. The interaction results in unsteady shock motion and a nonequilibrium turbulent boundary layer downstream and upstream of the interaction. Depending on the conditions, a separation bubble may develop in the region of shock impingement and a shock/shock interaction between the incoming and reflected shocks takes place at some distance from the wall. The shock/shock interaction produces a nonequilibrium mixing layer at the slip line, which is turbulent at high Reynolds numbers. Furthermore, the interaction of the slip layer and the turbulent boundary layer downstream of the interaction may lead to the development of underexpanded jets. We propose flow conditions where the incoming turbulent boundary layer is the same as the one used in the compression corner study described above. The incident shock will be generated by a deflection of 10°. Under these conditions, the combined pressure jump due to the incident and reflected shock will be similar to that seen in the compression corner study. The separated zone is also expected to be similar in size.

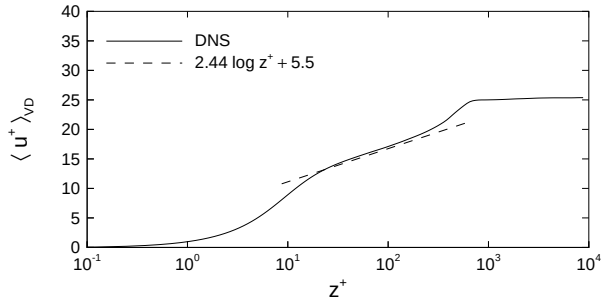

Fig. 1 Van-Driest transformed velocity scaled on inner variables for a DNS of a Mach 4, $Re_\theta = 9480$ adiabatic boundary layer.

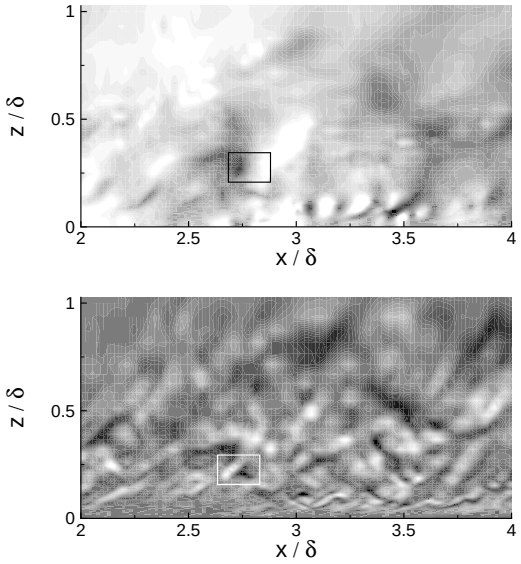

Fig. 2 DNS of a turbulent boundary layer at $M = 4$ and $Re_\theta = 9480$. Contours of (Top) pressure and (Bottom) divergence of the velocity on streamwise-wall-normal planes.

Case III: Swept fin interaction

This interaction will be at Mach 8 over a 5° sharp fin. The pressure ratio is expected to be about 3, and it is expected that the resulting interaction will be conical and grow in size along the shock direction. That is, the interaction is expected to display conical similarity so that the flow in the cross-section normal to the shock can be scaled in a conical coordinate system. The data for this case will be generated using large-eddy simulation (LES).

Computational Method

Generally, the computational study of shock/turbulence interaction has been done using shock fitting methods, where the location of the shock is guessed a priori and a special shock-capturing numerical technique is used in the identified shock region.[2,3] An alternative technique is the dynamic shock-capturing technique in which the entire field is computed using a weighted-essentially-non-oscillatory (WENO) scheme. Using this technique in smooth regions, the convective fluxes are represented by a symmetric stencil which provides high-order accuracy, high bandwidth and low dissipation.

We use a WENO scheme for the inviscid fluxes with an implicit time advancement technique. The third-order accurate, high-bandwidth, WENO scheme was designed for low dissipation and high bandwidth[4] and provides shock-capturing, which is necessary at the Mach numbers that we consider. The time advancement technique is based on the Data-Parallel Lower-Upper (DPLR) relaxation method of Candler *et al.*[5] and was extended to second-order accuracy by Olejniczak & Candler.[6] The derivatives required for the viscous terms are evaluated using 4th-order central differences. The codes include sub-grid scale (SGS) models[7] that can be turn off to perform DNS or on to perform LES.

Figure 1 shows the Van-Driest velocity profile for the DNS of a turbulent boundary layer at Mach 4. The Reynolds number based on the momentum thickness is $Re_\theta = 9480$. The results show good agreement with the theoretical and empirical predictions in the logarithmic region and viscous sublayer. The predictions given by the DNS data and the Van Driest II theory for the skin friction are within 2%.[8]

Figure 2 shows contours of pressure and divergence of velocity on the same boundary layer. The flow goes from left to right. The large gradients from positive to negative divergence correlated with large gradients of opposite sign in pressure illustrate the presence of shocklets. This is corroborated by computing the Rankine-Hugoniot conditions and ensuring that these are found in the turbulent flow field along the instantaneous streamline. The window in the figure shows the location of a shocklet, which is a small length scale, small time scale shock near the wall.

Shock-capturing techniques such as WENO schemes are too dissipative on coarse, LES-like grids, when applied directly. The WENO technique is based on the adaption of the differencing stencil near shocks. When using WENO schemes directly on a turbulent flow field, the adaption mechanism is based on the mathematical definition of data smoothness and has no information about the turbulence state. In LES grids the resolution is not fine enough for the adaption mechanism to distinguish between turbulent fluctuations and high-gradients associated with shocks. For this reason, we use a physically based shock sensor in combination with the mathematical WENO adaption technique. In this method additional information about the turbulence state is provided and the WENO scheme is only turned on dynamically in regions where

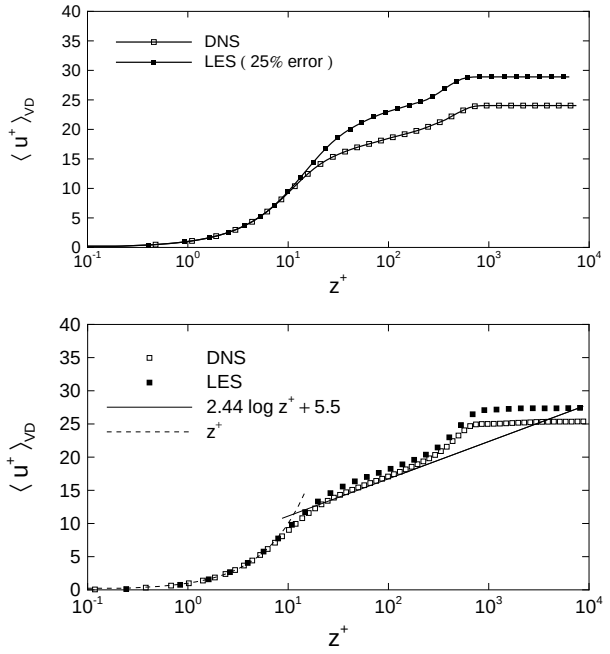

Fig. 3 LES of turbulent boundary layers at $M = 4$ and $Re_\theta = 9480$ for the adiabatic and isothermal simulation and comparing to the DNS result. The LES is performed using the WENO technique applied directly (Top) and the hybrid WENO technique using the mathematical and physical adaption mechanism (Bottom).

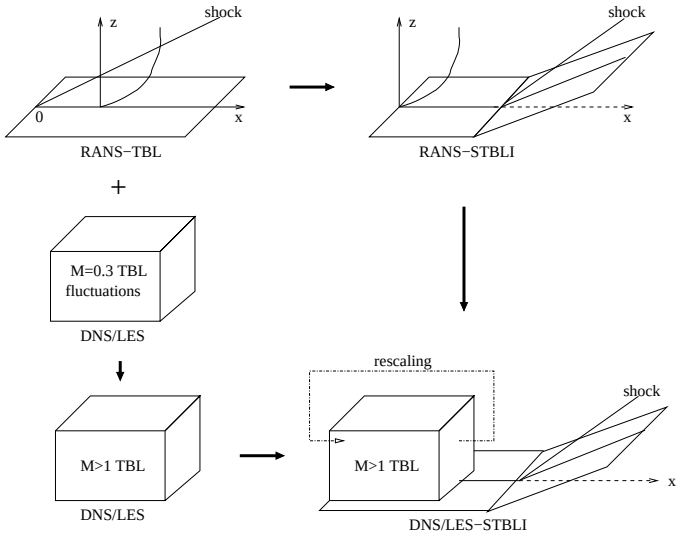

Fig. 4 Schematic of the initialization procedure for the STBLI simulations

shocks (based on the mathematical and physical definition) are present. Further details about the preliminary shock sensor can be obtained in Martin.[9] Figure 3 shows the LES results for a turbulent, adiabatic boundary layer at Mach 4 using a WENO scheme directly (Top) and the hybrid WENO plus shock sensor technique (Bottom). The DNS result is also shown for comparison. The magnitude of the van-Driest scaled velocity is overpredicted when the WENO is applied directly, whereas accurate data can be obtained using the hybrid method.

For LES, the conservative equations include five subgrid-scale terms that must be modeled:[7] the SGS stresses; SGS heat flux; SGS viscous diffusion; SGS viscous dissipation; and the redistribution of turbulent kinetic energy by the SGS scales or SGS turbulent kinetic energy diffusion. We use the SGS mixed models for compressible flow that are presented in Martin *et al.*[7] These models combine the scale-similarity assumption[10] with eddy viscosity models.[11] The models include a dynamic evaluation of the model coefficients.[12] At present, we are assessing the performance of this method to simulate shock-wave/turbulent boundary layer interactions.

Initialization

The initial flow fields are obtained combining the results from different simulations. We first simulate a turbulent boundary layer at the desired conditions. We then place the DNS simulation of the turbulent boundary layer as the upstream condition for the STBLI. This procedure is explained below.

We first obtain the mean turbulent flow for the incoming turbulent boundary layer, RANS-TBL from here on, using a Balwin-Lomax Reynolds-averaged Navier-Stokes simulation.[13] The resulting mean profiles are then used as the mean flow for the DNS/LES simulation of a turbulent boundary layer. The fluctuating velocity field is obtained by normalizing the velocity fluctuations from the incompressible Mach 0.3 DNS[14] by the ratio of the inner parameters at the high Mach number to that at M =0.3. The turbulent field is mapped onto a computational domain that is also normalized in wall units. Thus, the initial turbulent structures and energy spectra resemble those of a realistic turbulent boundary layer. Our preliminary experience with Mach 8 turbulent boundary layer simulations is that this initialization procedure may allow for short simulation transients provided that the RANS-TBL calculation is accurate. The initial fluctuations in the thermodynamic variables are estimated using the strong Reynolds analogy.[15]

The RANS-TBL is then used as the inflow boundary condition for a second RANS calculation to simulate the STBLI mean flow. The result from this simulation together with the DNS/LES of the inflow turbulent boundary layer form the initial condition for the STBLI direct numerical or large-eddy simulation.

Figure 4 shows a schematic of the initialization procedure.

Grid Generation

For each of the three canonical STBLI cases, a 2D plane of the physical domain is closed by two curves

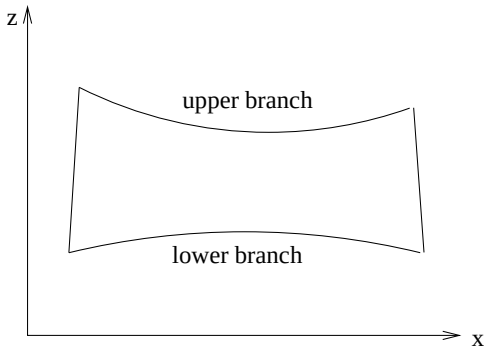

Fig. 5 Schematic of a physical domain for STBLI.

and two straight lines, as illustrated in Fig. 5. Following Adams,[16] two-step analytical transformations are used to map the physical domain onto a computational domain. The computational domain is discretized by a uniform mesh, which is transformed to the physical mesh of the physical domain. In the first step, a parameter $s \in [0,1]$ is introduced to describe the upper and lower curves of the physical domain as

$$\begin{cases} x_l = x_l(s),\ z_l = z_l(s) \\ x_u = x_u(s),\ z_u = z_u(s) \end{cases}, \tag{1}$$

where subscripts l and u represent the lower and upper curves. Then, a linear transformation is used to map the physical domain (x, z) onto the intermediate domain $(s, r) \in [0,1] \times [0,1]$ as

$$\begin{cases} x(r,s) = (1-r)x_l(s) + rx_u(s) \\ z(r,s) = (1-r)z_l(s) + rz_u(s) \end{cases}. \tag{2}$$

In the second step, the intermediate domain (r, s) is mapped onto the computational domain $(\xi, \zeta) \in [0,1] \times [0,1]$. The transformation is given by

$$\begin{cases} s = s(\xi) \\ r = r(\zeta) \end{cases}, \tag{3}$$

where functions $s(\xi)$ and $r(\zeta)$ are constructed to control the grid distribution of the physical mesh.

Fig. 6 shows the physical meshes for Case I (every 40th line in x, every 15th line in z), Case II (every 36th line in x, every 5th line in z) and Case III (every 72th line in x, every 9th line in y). It can be seen that all grids are clustered near the walls and around corners.

Case I: compression ramp

The schematic of the physical domain for the compression ramp is shown in Fig.7. The mathematical description of the lower curve is

$$x_l(s) = L_l \cdot s, \quad z_l(s) = d_{2l}x_l(s) + \frac{d_{2l}}{d_{1l}} \ln\{\cosh[d_{1l}(x_l(s) - x_{cl})]\} + d_{2l}d_{3l} \tag{4}$$

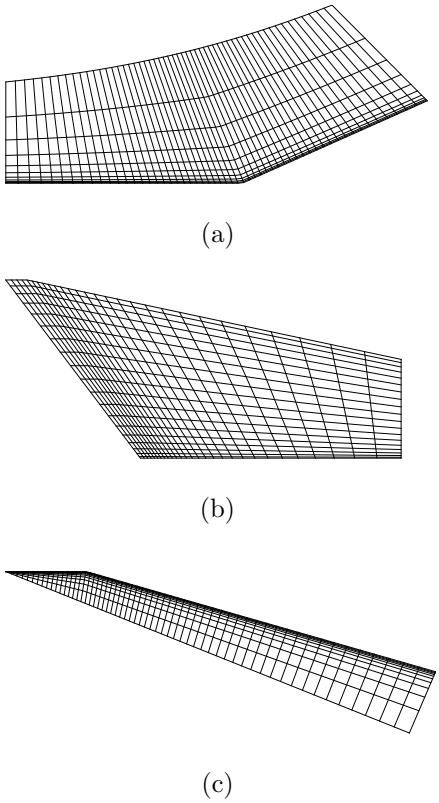

Fig. 6 Grids for (a) compression ramp on a streamwise/wall-normal plane, (b) reflected shock case with separation and turbulent slip layer on a streamwise/wall-normal plane and (c) swept fin interaction case on a streamwise/spanwise plane.

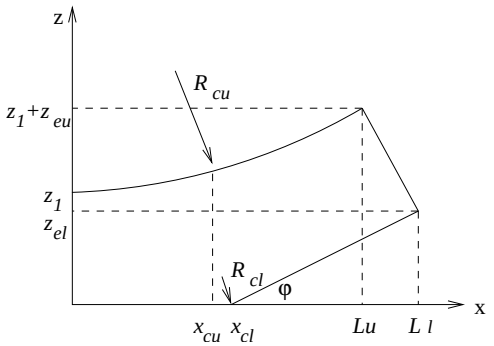

Fig. 7 Schematic of the compression ramp.

where

$$\begin{aligned} d_{1l} &= \frac{\left(1 + d_{2l}^2\right)^{3/2}}{R_{cl}}, \\ d_{3l} &= -\frac{1}{d_{1l}} \ln[\cosh(d_{1l}x_{cl})], \end{aligned} \tag{5}$$

in which R_{cl} is the curvature at corner $(x_{cl}, 0)$, d_{2l} is obtained by solving $z_l(s = 1) = z_{el}$, and all of the other symbols are defined in Fig. 7. In the same way

as the lower curve, the upper curve is described as

$$x_u(s) = L_u \cdot s, \quad z_u(s) = z_1^+ d_{2u} x_u(s) + \frac{d_{2u}}{d_{1u}} \ln\{\cosh[d_{1u}(x_u(s) - x_{cu})]\} + d_{2u} d_{3u} \tag{6}$$

where

$$\begin{aligned} d_{1u} &= \frac{\left(1 + d_{2u}^2\right)^{3/2}}{R_{cu}}, \\ d_{3u} &= -\frac{1}{d_{1u}} \ln[\cosh(d_{1u} x_{cu})], \end{aligned} \tag{7}$$

in which R_{cu} is the curvature at $x = x_{cu}$ and d_{2u} is obtained by solving $z_u(s = 1) = z_1 + z_{eu}$.

Function $s(\xi)$ is chosen to be

$$s(\xi) = a\xi + b + c_1 \sinh\left[g(\xi)\right], \quad g(\xi) = \frac{\xi - c_2}{c_3}, \tag{8}$$

where

$$a = 1 - c_1 \left[\sinh\left(\frac{c_2}{c_3}\right) + \sinh\left(\frac{1 - c_2}{c_3}\right)\right], \tag{9}$$

$$b = c_1 \sinh\left(\frac{c_2}{c_3}\right). \tag{10}$$

Parameters c_1 and c_3 are specified to cluster the physical mesh at $\xi = c_2$. Increasing c_1 or decreasing c_3 makes physical mesh more clustered at $\xi = c_2$. We want the mesh clustered at $x = x_{cl}$ in the x-direction. Thus, we get the following equation to solve c_2 :

$$x_{cl} = x_l\left[s(\xi = c_2)\right]. \tag{11}$$

Function $r(\zeta)$ is chosen to be

$$r(\zeta) = \frac{cc \cdot h_1(\zeta)}{aa + bb \cdot h_1(\zeta)} \tag{12}$$

where

$$\begin{aligned} h_1(\zeta) &= c\zeta + d + e_1 sinh\left[h_2(\zeta)\right], \quad (13) \\ h_2(\zeta) &= \frac{\zeta - e_2}{e_3}, \quad (14) \end{aligned}$$

in which

$$c = 1 - e_1 \left[\sinh\left(\frac{1 - e_2}{e_3}\right) + \sinh\left(\frac{e_2}{e_3}\right)\right] \tag{15}$$

$$d = e_1 \sinh\left(\frac{e_2}{e_3}\right). \tag{16}$$

Parameters e_1 and e_3 have the same effects as c_1 and c_3. Increasing e_1 or decreasing e_3 makes the physical mesh clustered at $\zeta = e_2$. We want the physical mesh to be clustered at the lower boundary. Therefore e_2 is set to be zero. Parameters *aa*, *bb* and *cc* are used to control that half of the grid lines in the z direction lie in the range $z \in [0, z_{12}]$ at $x = 0$. They are computed by

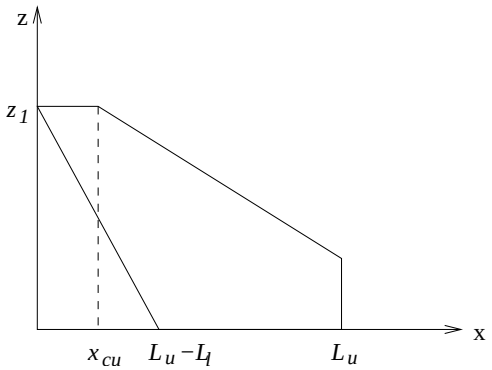

Fig. 8 Schematic of the slip layer.

$$aa = h_1(0.5) \cdot \left(1 - \frac{z_{12}}{z_1}\right), \tag{17}$$

$$bb = \left(\frac{z_{12}}{z_1} - h_1(0.5)\right), \tag{18}$$

$$cc = \frac{z_{12}}{z_1}\left(1 - h_1(0.5)\right). \tag{19}$$

Case II: reflected shock with separation and turbulent slip layer

The schematic of the physical domain for this case is shown in Fig.8. The upper and lower curves are

$$\begin{cases} x_l(s) = (L_u - L_l) + L_l s, \quad z_l(s) = 0 \\ x_u(s) = L_u s, \quad z_u(s) = z_1 - (d_{2u} x_u(s) + \\ \frac{d_{2u}}{d_{1u}} \ln\{\cosh[d_{2u}(x_u(s) - x_{cu})]\} + d_{2u} d_{3u}) \end{cases} \tag{20}$$

where parameters d_{1u}, d_{2u} and d_{3u} are computed as in the ramp case. The forms of functions $s(\xi)$ and $r(\zeta)$ are also the same as in the ramp case, but $h_1(\zeta)$ in the expression of function $r(\zeta)$, see Eq. (12), takes a different form as

$$h_1(\zeta) = c\zeta + d + e_1 \tanh\left[h_2(\zeta)\right]. \tag{21}$$

We use hyper-tangent function $\tanh(\cdot)$ in Eq. (21) to make the physical mesh clustered near the both walls. Increasing e_1 or decreasing e_3 makes the physical mesh more clustered near the both walls. At $\zeta = e_2$ the mesh is coarsest.

Case III: swept fin

Referring to Fig. 9, the lower and upper curves in this case are described as

$$\begin{cases} x_l(s) = L_l \cdot s, \quad y_l(s) = y_1(1 - s) \\ x_u(s) = L_u \cdot s, \quad y_u(s) = y_1 - (d_{2u} x_u(s) + \\ \frac{d_{2u}}{d_{1u}} \ln\{\cosh[d_{1u}(x_u(s) - x_{cu})]\} + d_{2u} d_{3u}) \end{cases} \tag{22}$$

where d_{1u}, d_{2u} and d_{3u} are computed as in the ramp case. Functions $s(\xi)$ and $r(\eta)$ are also the same as in the ramp case.

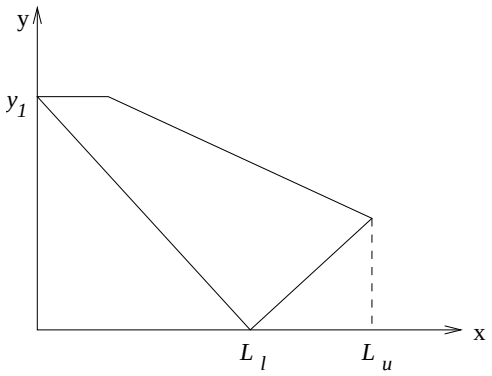

Fig. 9 Schematic of the swept fin.

Inflow Methodology

To numerically simulate the shock/turbulent boundary layer interaction in the three canonical cases, we need inflow/outflow boundary conditions. We use a sponge layer[16,17] in combination with non-reflecting boundary conditions to handle the outflow. Extending the work by Lund *et al.*,[18] we propose a rescaling method[19] which generates compressible turbulent inflow efficiently and accurately. The method assumes that, in the coming boundary layers of the three canonical cases, the compressibility effects reduce to density variation effects and general temperature-velocity relationships exist. To generate the inflow data, we rescale the downstream profile and reintroduce it at the inlet. Due to the presence of multiple length scales in a turbulent boundary layer, the rescaling process is carried out in a piecemeal fashion. To rescale the mean streamwise velocity, we follow Ref. 20 and distinguish the viscous sublayer, the logarithmic region and the law-of-the-wake region in the boundary layer. To rescale the mean wall-normal velocity and turbulence, we divide the boundary layer into the inner layer and outer layer. Hereafter, we denote the streamwise, spanwise and wall-normal velocity components as $u(= U + u')$, $v(= V + v')$ and $w(= W + w')$, where a capital letter represents a time-averaged mean, and a lowercase letter with prime represents a fluctuation. We use $(\cdot)_i$ and $(\cdot)_r$ to represent the inlet and the rescaled downstream station respectively.

Mean rescaling

For a flat-plate boundary layer, the mean spanwise velocity V is zero due to the spanwise statistical symmetry, and the mean pressure P is equal to the free stream value. Thus, the remaining mean variables to be rescaled are the mean streamwise velocity U, the mean wall-normal velocity W, the mean temperature T and the mean density $\bar{\rho}$.

In the viscous sublayer, the logarithmic region and the law-of-the-wake region, the mean streamwise velocity respectively satisfies the following scaling laws

$$\frac{U^s}{u_\tau} = f_{\text{visc}}(z^+), \tag{23}$$

$$\frac{U^{**}}{u_\tau} = f_{\log}(z^+), \tag{24}$$

$$\frac{U^*}{u_\tau} = f_{\text{wake}}(\eta), \tag{25}$$

where $u_\tau = \sqrt{\left(\nu \frac{\partial U}{\partial z}\right)_w}$ is the friction velocity, $z^+ = \frac{u_\tau z}{\nu_w}$ is the wall-normal coordinate in viscous length units, $\eta = \frac{z}{\Delta}$ is the wall-normal coordinate nondimensinalized by an integral reference length scale, Δ; The functions f_{visc}, $f_{\log}$ and f_{wake} are independent of the streamwise location; and U^s, U^{**} and U^* are forms of the transformed mean streamwise velocity and are defined as

$$U^s = \int_0^U \left(\frac{T}{T_w}\right)^n \mathrm{d}U, \tag{26}$$

$$U^{**} = \int_0^U \sqrt{\frac{T_w}{T}} \mathrm{d}U, \tag{27}$$

$$U^* = U_e^{**} - U^{**} = \int_U^{U_e} \sqrt{\frac{T_w}{T}} \mathrm{d}U, \tag{28}$$

where n comes from the power law relation between viscosity and temperature

$$\frac{\mu}{\mu_w} = \left(\frac{T}{T_w}\right)^n. \tag{29}$$

Applied at the inlet and the rescaled station, Eq. (23) and (24) respectively give

$$(U^s)_i = \omega_{u_\tau} (U^s)_r, \tag{30}$$

$$(U^{**})_i = \omega_{u_\tau} (U^{**})_r \tag{31}$$

for $(z^+)_i = (z^+)_r$ in the viscous sublayer and the logarithmic region, and Eq. (25) gives

$$(U^*)_i = \omega_{u_\tau} (U^*)_r \tag{32}$$

for $(\eta)_i = (\eta)_r$ in the law-of-the-wake region, where ω_{u_τ} is defined as

$$\omega_{u_\tau} = \frac{(u_\tau)_i}{(u_\tau)_r}. \tag{33}$$

In the inner and the outer layers of the boundary layer, the mean wall-normal velocity W is assumed to be scaled as

$$\frac{W}{u_\tau}\sqrt{\frac{\bar{\rho}}{\bar{\rho}_w}} = f_{\text{inner}}(z^+), \tag{34}$$

$$\frac{W}{u_\tau}\sqrt{\frac{\bar{\rho}}{\bar{\rho}_w}} = f_{\text{outer}}(\eta), \tag{35}$$

where functions f_{inner} and f_{outer} are assumed to be independent of streamwise location. Applied at the rescaled station and the inlet, the scaling of W leads to

$$(W)_i = \omega_{u_\tau}\omega_{\rho_w}\frac{(\bar{\rho})_r}{(\bar{\rho})_i}(W)_r, \tag{36}$$

for $(z^+)_r = (z^+)_i$ in the inner layer and $(\eta)_r = (\eta)_i$ in the outer layer. ω_{ρ_w} is given by

$$\omega_{\rho_w} = \frac{(\bar{\rho}_w)_i}{(\bar{\rho}_w)_r}. \tag{37}$$

When fluctuations are small, to a first-order approximation, the mean temperature T and the mean density $\bar{\rho}$ are related by the state equation $T = \frac{P}{R\bar{\rho}}$ for perfect gas, where R is the gas constant. Thus, the rescaling of $\bar{\rho}$ follows once that of the mean temperature T is known.

If the streamwise distance from the rescaled station to the inlet is not very large, it is a good assumption that the relationship between the mean temperature and the mean streamwise velocity is the same at the two locations. We therefore have

$$\frac{T}{T_e} = f_{UT}\left(\frac{U}{U_e}\right), \tag{38}$$

where subscript e denotes a quantity in the free stream, f_{UT} is a function independent of the streamwise location. For a boundary layer under non-zero pressure gradient, the relationship in Eq. (38) may not take the same form as Walz's equation, but its form is not needed as far as the rescaling method is concerned. We can obtain the relationship numerically at the rescaled station and then use interpolation to decouple the mean streamwise velocity and the mean temperature in the computation of the mean streamwise velocity at the inlet. The mean temperature at the inlet follows Eq. (38) once the mean streamwise velocity at the inlet is calculated.

Turbulence rescaling

When the velocity fluctuations are normalized by the Morkovin velocity scaling $\sqrt{\frac{\bar{\rho}_w}{\bar{\rho}}}u_\tau$, they are in fair agreement with the incompressible data. Applied at the rescaled station and the inlet, the scaling of u_i' ($i = 1, 2, 3$ corresponding to u',v',w') leads to

$$(u_i')_i = \omega_{u_\tau}\omega_{\rho_w}\frac{(\bar{\rho})_r}{(\bar{\rho})_i}(u_i')_r, \tag{39}$$

for $(z^+)_r = (z^+)_i$ in the inner layer and $(\eta)_r = (\eta)_i$ in the outer layer.

$$(T_w'(t))_i = \frac{\omega_{\rho_w}\omega_{\nu_w}}{\omega_{u_\tau}}\frac{(\bar{\rho})_r}{(\bar{\rho})_i}\frac{(T_w)_i}{(T_w)_r}(T_w'(t))_r. \tag{40}$$

To a first-order approximation, the state equation yields

$$\frac{p'}{P} = \frac{T'}{T} + \frac{\rho'}{\bar{\rho}}. \tag{41}$$

In most cases, $\frac{p'}{P}$ is very small and can be assumed to be negligible, which gives

$$\frac{\rho'}{\bar{\rho}} = -\frac{T'}{T}. \tag{42}$$

Thus, only the temperature fluctuations need to be rescaled.

We treat the rescaling of temperature fluctuations in the same way as we deal with the mean temperature. We assume the following relations

$$\frac{T_{\text{rms}}}{T} = f_{\text{amp}}\frac{u_{\text{rms}}}{U}, \tag{43}$$

$$\frac{T'(t)}{T_{\text{rms}}} = c\frac{u'(t + f_{\text{phase}})}{u_{\text{rms}}}, \tag{44}$$

where t denotes time, c is equal to $+1$ (or -1) where u' and T' are positively (or negatively) correlated, f_{amp} and f_{phase} are functions of z^+ in the inner layer and η in the outer layer, and they are not functions of the streamwise location. Applying Equations (43) and (44) to the rescaled station and the inlet, we can deduce

$$\begin{aligned}(T'(t))_i &= \frac{(u'(t + f_{\text{phase}}))_i}{(u'(t + f_{\text{phase}}))_r}\frac{(U)_r}{(U)_i}\frac{(T)_i}{(T)_r}(T'(t))_r \\ &= \omega_{u_\tau}\omega_{\rho_w}\frac{(\bar{\rho})_r}{(\bar{\rho})_i}\frac{(U)_r}{(U)_i}\frac{(T)_i}{(T)_r}(T'(t))_r. \end{aligned}\tag{45}$$

Approaching the wall, $\frac{(U)_r}{(U)_i}$ becomes a $\frac{0}{0}$ type limit and can be evaluated according to L'Hospital rule.

Implementation

In the rescaling of the mean streamwise velocity, three sublayers are distinguished. In the rescaling of other quantities, the boundary layer is divided into the inner sublayer and the outer sublayer. The composite profile of a quantity over the entire boundary layer is formed by a weighted combination of the profiles for all sublayers. For example, the streamwise velocity is formed as

$$\begin{aligned}u = \{U_{\text{visc}}b_1(z) + U_{\log}b_2(z) + U_{\text{wake}}b_3(z)\} + \\ \{u'_{\text{inner}}[1 - b_3(z)] + u'_{\text{outer}}b_3(z)\},\end{aligned}\tag{46}$$

where U_{visc}, $U_{\log}$ and U_{wake} represent the mean profiles in the viscous sublayer, the logarithmic region and the wake region respectively, u'_{inner} and u'_{outer} in turn represent the fluctuation profiles in the inner layer and the outer layer, and $b_1(z)$, $b_2(z)$ and $b_3(z)$ are weight functions. The weight functions are constructed from

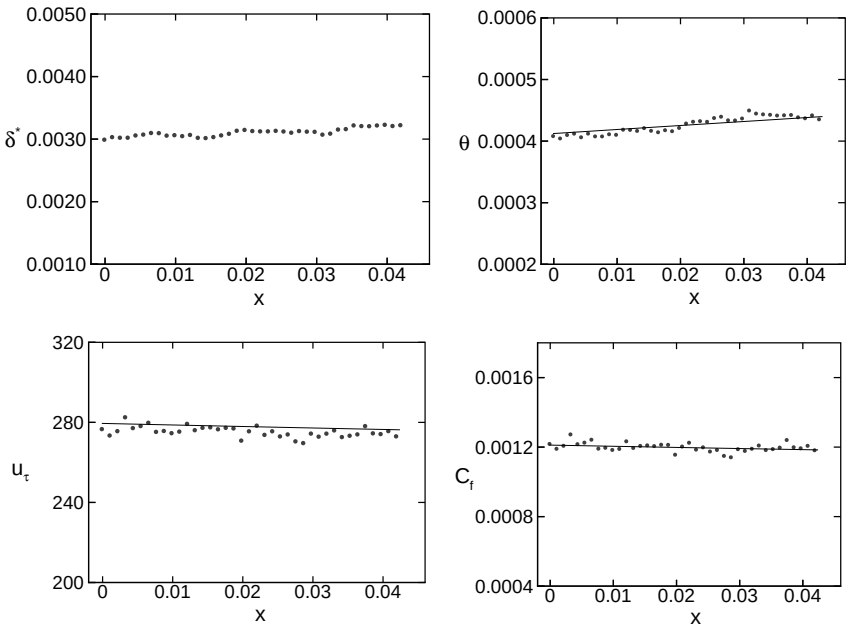

Fig. 10 Distributions of the displacement thickness δ^*, momentum thickness θ, friction velocity u_τ and friction coefficient C_f along the streamwise (x) direction. solid circles: SDNS, dashed lines: initial periodic flow field, solid lines: formulas from Least Square (LS) minimization.

hyper-tangent functions as

$$b_1(k) = \frac{1}{2}\left\{1 - \tanh\left[c_1 \frac{k - k_{m1}}{k_{\rm logs} - k_{\rm visc}}\right]\right\}, \quad (47)$$

$$b_2(k) = \frac{1}{2}\left\{\tanh\left[c_1 \frac{k - k_{m1}}{k_{\rm logs} - k_{\rm visc}}\right] - \tanh\left[c_{23} \frac{k - k_{m23}}{k_{\rm wake} - k_{\rm loge}}\right]\right\}, \quad (48)$$

$$b_3(k) = \frac{1}{2}\left\{1 + \tanh\left[c_{23} \frac{k - k_{m23}}{k_{\rm wake} - k_{\rm loge}}\right]\right\}, \quad (49)$$

where k is the wall-normal grid index and equivalent to coordinate z, c_1 and c_{23} are constants to adjust the steepness of the weight functions, $k_{\rm visc}$, $k_{\rm logs}$, $k_{\rm loge}$ and $k_{\rm wake}$ are the wall-normal indexes to distinguish different sublayers, $k_{m1} = \frac{k_{\rm visc}+k_{\rm logs}}{2}$ and $k_{m23} = \frac{k_{\rm loge}+k_{\rm wake}}{2}$.

Test

The rescaling method can be used to simulate a spatially developing turbulent boundary layer. Fig. 10 shows the spatial evolution of the boundary layer displacement thickness δ^*, momentum thickness θ, friction velocity u_τ and friction coefficient C_f in a spatially developing turbulent boundary layer direct numerical simulation (SDNS). The solid circles represent the time-averaged spatial distributions of these quantities for the spatial boundary layer in equilibrium.

Fig. 11(a) shows that the streamwise evolution of Re_θ from the simulation is in excellent agreement with the one estimated by Sivells & Payne formula under van Driest II transformation.[21] We use Least Square (LS) minimization to produce a formula similar to

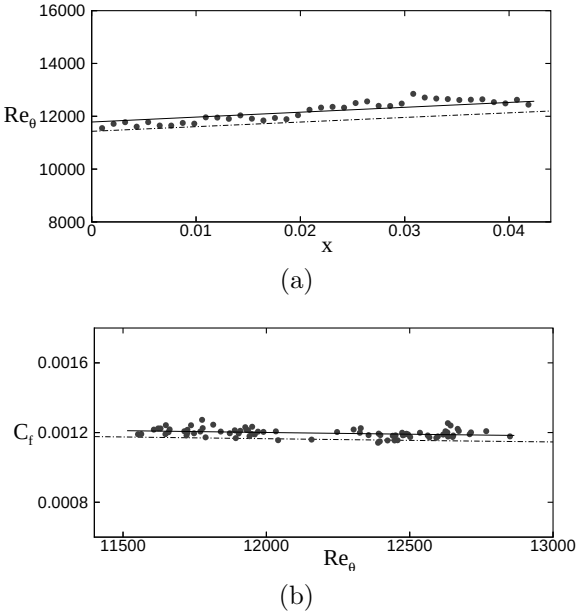

(a)

(b)

Fig. 11 (a)Distribution of Re_θ along the streamwise direction and (b) Distribution of the local skin friction C_f in terms of Re_θ. solid circles: simulation, dashdotted line: estimation by theoretical equations, solid line: formula from Least Square (LS) minimization.

Sivells & Payne formula under van Driest II transformation. The solid line in Fig. 11 represents the plot from the LS minimization.

Fig. 11(b) compares the simulated local skin friction C_f in terms of Re_θ with the estimation by Karman-

Schoenherr equation under van Driest II transformation.[21] The dashdotted line is plotted from the estimation, solid circles denote time-averaged values from the spatial simulation. The solid line represents the results of the LS minimization. As indicated by the comparison, the result from the simulation is in good agreement with the estimation.

The rescaling procedure will be used to provide the inflow boundary condition for the simulations of shockwave turbulent boundary layer interaction. Further details about this method can be found in Xu & Martin.[19]

Conclusions

The initial progress on the development of a detailed DNS and LES database of shockwave turbulent boundary layer interaction is presented. The canonical configurations that are chosen and the grid generation procedure for these configurations are described. The validation of the computational codes, the flow initialization procedure and the inflow generation methodology are given. There is much work to be done prior to using the database to gain physical understanding. In particular, future work involves finishing the initialization of the Mach 3 and 8 boundary layers, gaining experience using the inflow methodology for this type of flow and using the WENO scheme to compute the flows in the prescribed grids, and assessing the performance of the LES models in STBLI.

Acknowledgments

We would like to thank NASA Ames for the use of the DPLR CFD code to generate the turbulent mean flow, and to Michael Wright at ELORET for his guidance in how to use this code. This work is supported by the Air Force Office of Scientific Research under grant AF/F49620-02-1-0361 and the National Science Foundation under grant # CTS-0238390.

References

[1]Evans, T. and Smits, A., "Measurements of the Mean Heat Transfer in a Shock Wave Turbulent Boundary Layer Interaction," *Experimental Thermal and Fluid Science*, 12, 1993, pp. 87–97.

[2]Adams, N. A., "Direct simulation of the turbulent boundary layer along a compression ramp at $M = 3$ and $Re_\theta = 1685$," *J. Fluid Mech.*, Vol. 420, 2000, pp. 47–83.

[3]Rizzetta, D., Visbal, M., and Gaitonde, D., "Large-Eddy Simulation of Supersonic Compression-Ramp Flow by High-Order Method," *AIAA J.*, Vol. 39, No. 12, 2001, pp. 2283–2292.

[4]Weirs, V. and Candler, G., "Optimization of weighted ENO schemes for DNS of compressible turbulence," *AIAA Paper No. 97-1940*, 1997.

[5]Candler, G., Wright, W., and McDonald, J., "Data-Parallel Lower-Upper Relaxation method for reacting flows," *AIAA Journal*, Vol. 32, 1994, pp. 2380–2386.

[6]Olejniczak, D. and Candler, G., "Hybrid finite-difference methods for DNS of compressible turbulent boundary layers," *AIAA Paper No. 96-2086*, 1996.

[7]Martin, M., Piomelli, U., and Candler, G., "Subgrid-Scale Models for Compressible LES," *Theoretical and Computational Fluid Dynamics*, Vol. 13, 2000, pp. 361–376.

[8]Martin, M. P., "DNS database of hypersonic turbulent boundary layers," *AIAA Paper No. 03-3726*, 2003.

[9]Martin, M., "Shock capturing and the LES of high-speed flows," *Annual Research Briefs, Center for Turbulence Research*, 2000.

[10]Bardina, J., Ferziger, J., and Reynolds, W., "Improved subgrid-scale models for large eddy simulation," *AIAA Paper No. 80-1357*, 1980.

[11]Smagorinsky, J., "General Circulation Experiments with the Primitive Equations. I. The Basic Experiment," *Monthly Weather Review*, Vol. 91, 1963, pp. 99–164.

[12]Moin, P., Squires, K., Cabot, W., and Lee, S., "A dynamic subgrid-scale model for compressible turbulence and scalar transport," *Physics of Fluids*, Vol. 3, 1991, pp. 2746–2757.

[13]DPLR, CFD, and Code, *NASA Ames Research Center, Moffett Field, CA*, 2003.

[14]Martin, M., Olejniczak, D., Weirs, G., and Candler, G., "DNS of reacting hypersonic boundary layers," *AIAA Paper No. 98-2817*, 1998.

[15]Morkovin, M., "Effects of compressibility on turbulent flows," *A.J. (ed) of Mèchanique de la Turbulence, CNRS*, 1962, pp. 367–380.

[16]Adams, N. A., "Direct numerical simulation of turbulent compression ramp flow," *Theoret. Comput. Fluid Dynamics*, Vol. 12, 1998, pp. 109–129.

[17]Guo, Y., Adams, N., and Kleiser, L., "A comparison study of an improved temporal DNS and spatial DNS of compressible boundary layer transition," *AIAA J.*, Vol. 34, 1996, pp. 683–690.

[18]Lund, T., Wu, X., and Squires, K., "Generation of turbulent inflow data for spatially-developing boundary layer simulations," *J. Comput. Phys.*, Vol. 140, 1998, pp. 233–258.

[19]Xu, S. and Martin, M., "Inflow boundary conditions for the simulation of compressible turbulent boundary layers," *AIAA Paper No. 2003-3963*, 2003.

[20]Smits, A. and Dussauge, J., *Boundary Layer Mean-Flow Behavior*, AIP PRESS, 1996, In Turbulent Shear Layers in Supersonic Flows.

[21]Hopkins, E. and Inouye, M., "An evaluation of theories for predicting turbulent skin friction and heat transfer on flat plates at supersonic and hypersonic Mach numbers," *AIAA J.*, Vol. 9, No. 6, 1971, pp. 993–1003.